Applied Thermal Engineering 231 (2023) 120845

Contents lists available at ScienceDirect

Applied Thermal Engineering

journal homepage: www.elsevier.com/locate/ate

Research Paper

Thermoacoustic engines with near-critical working fluids

Nathan Blanc [a], Rui Yang [b,*], Guy Z. Ramon [a], Ercang Luo [b,c]

[a] The Nancy and Stephen Grand Technion Energy Program and Department of Civil & Environmental Engineering, Technion – Israel Institute of Technology, Haifa 32000, Israel

[b] CAS Key Laboratory of Cryogenics, Technical Institute of Physics and Chemistry, Chinese Academy of Sciences, Beijing 100190, China

[c] University of Chinese Academy of Sciences, No. 19 Yuquan Rd., Beijing 100049, China

ARTICLE INFO

Keywords:
Thermoacoustic engine
Critical point
Near-critical fluids
Low-grade heat

ABSTRACT

Thermoacoustic engines are devices in which heat is converted into acoustic oscillations, which can be tuned to mimic the thermodynamic cycle executed by mechanical motion such as that of a piston. In classical thermoacoustics, the working fluid is a gas far from the critical point. Herein, we extend the scope of working fluids to theoretically examine thermoacoustic conversion with fluids near their critical points. First, a "short engine" approximation is used, in which the acoustic field is assumed to be uniform and standing-wave dominated. This is then followed by a full-scale model of a standing-wave engine. Both models are investigated via the numerical solution of the equations for linear thermoacoustics, supplemented by the non-ideal equation of state for all fluid properties. The numerical model was first validated against published experimental results, and then used to project performance characteristics under various conditions. Results demonstrate that under operating conditions close to the critical point, thermoacoustic conversion can be enhanced; however, acoustic dissipation also increases, resulting in a trade-off between the larger output power of the engine (at a lower temperature difference) and the efficiency, which decreases. Importantly, the sub-critical region (i.e., at a pressure slightly lower than the critical pressure) yields better performance than the supercritical region in terms of both power output and efficiency. A potential application of near-critical thermoacoustic engines is low-grade heat recovery, due to the lower temperature difference required to drive the engine compared to classical engines.

1. Introduction

Thermoacoustic engines can convert heat into acoustic power, with advantages of high reliability, low maintenance and potentially high efficiency [1,2]. Since the development of the high-performance thermoacoustic engine at the end of last century by Backhaus and Swift [3], many thermoacoustic electricity generation and refrigeration systems have been built. Some of them were reported to have efficiencies as high as those in traditional engines [4,5]. In recent years, thermoacoustic engines with a looped resonator and multiple stages have been intensively studied, which has extended the application of thermoacoustic technology into low-grade heat recovery [6,7]. In these systems, however, the efficiency and the power density are still lower than the commercially available technologies, e.g., organic Rankine cycles, in this temperature range. Since the distribution of acoustic field in these systems is often close to ideal (see e.g. Al-Kayiem and Yu [8], Chen and Xu [9]), the room for further improving the performance is increasingly narrower, which prevents their large-scale application.

Generally speaking, thermoacoustic phenomena may occur when a compressible fluid is thermally perturbed [10]. Such phenomena are much more significant in fluids near the critical point than those far away from the critical point, due to the sudden change of thermophysical properties including density, thermal conductivity, viscosity, etc [11]. For example, in gas turbine engines, when the cold fuel flows through the tubes inside the engine for cooling, high-amplitude pressure oscillations may occur if the state of the fluid is close to the critical point [12–14]. Another example is the widely-known piston effect, which leads to very fast heat transfer in a low-heat-diffusing, near-critical fluids confined in a cavity [15–20].

Encouraged by the above-mentioned thermoacoustic phenomena in fluids near the critical point, it is reasonable to deduce that near-critical fluids may be used in thermoacoustic engines to enhance the energy conversion. Actually, this idea has already been suggested in 1980s by Wheatley et al. [21] and Swift [22], and later by Jin et al. [23]. The credit of the development of the first trans-critical thermoacoustic engines should be given to Scalo's group in Purdue University [24–28]. Specifically, their first attempt is an engine with a half wavelength resonator of 1-m length. Damped oscillations were observed when

* Corresponding author.
E-mail address: yangrui@mail.ipc.ac.cn (R. Yang).

https://doi.org/10.1016/j.applthermaleng.2023.120845
Received 16 January 2023; Received in revised form 22 April 2023; Accepted 20 May 2023
Available online 14 June 2023

the system was excited by an external perturbation with the working fluid in a transcritical condition. Recently, this system was improved by adding a hot cavity, using more effective heat exchangers, and a locally enlarged thermoacoustic core [26,27]. R-218, whose critical temperature and pressure are 345.1 K and 2.64 MPa respectively, was selected as the working fluid. In the experiments, steady-state oscillations occurred with a temperature difference as low as 79 K. Due to the significant variation of density near the critical point, a peak-to-peak pressure amplitude as high as 669 kPa was achieved, with a mean pressure of 3.43 MPa (1.3 p_{cr}), and a temperature difference of 150 K along the stack. This amplitude is much higher than the amplitude that can be achieved in a classical thermoacoustic engine with similar temperature differences, showing the potential of trans-critical thermoacoustic engines as devices for energy extraction and waste heat removal. Additionally, high-order compressible Navier–Stokes simulations on trans-critical engines were conducted by Migliorino and Scalo [24,25], which reveal a boost of thermoacoustic conversion, as well as the required input heat, near the critical point.

To the authors' knowledge, the studies by Scalo's group are the only experimental explorations on thermoacoustic engines adopting near-critical (or trans-critical) fluids. To date, the mechanism of thermoacoustic conversion near the critical point stays unclear; the characteristics and the potential in performance of the thermoacoustic engine using near-critical fluids still lack study. Herein, we present a systematic theoretical study on a near-critical thermoacoustic engine, especially in a standing-wave field, through both an idealized short engine model and a full-scale standing-wave engine model. In the analysis of the short engine model, the main factors determining the near-critical thermoacoustic conversion are investigated, shedding light on the performance of an ideal standing-wave near-critical thermoacoustic engine. In the analysis of the full-scale engine, calculations are performed to show the effects of the near-critical fluid on a practical engine. Our results demonstrate that the utilization of a near-critical fluid can improve the acoustic power output, reduce the required temperature difference but decrease the efficiency.

2. Model formulation

Two models, including a short engine and a full-scale standing-wave engine, will be used to predict the performance of thermoacoustic conversion with near-critical fluids. They will be introduced in this section.

2.1. Governing equations

The governing equations describing the fluid thermoacoustic conversion have been derived by Swift et al. [29] based on Rott's acoustic assumptions [30]. They consist of the momentum equation, continuity equation, total energy flux equation and energy balance equation:

$$\frac{dp_1}{dx} = -\frac{i\omega\rho_m}{\left(1-f_v\right)A_g}U_1 \tag{1}$$

$$\frac{dU_1}{dx} = -\frac{i\omega A_g}{\rho_m a^2}\left[1+\frac{(\gamma-1)f_\kappa}{1+\epsilon_s}\right]p_1 + \frac{\beta\left(f_\kappa-f_v\right)}{\left(1-f_v\right)(1-Pr)(1+\epsilon_s)}\frac{dT_m}{dx}U_1 \tag{2}$$

$$\frac{dT_m}{dx} = \frac{\dot{H}_2 - \frac{1}{2}\Re\left[p_1\tilde{U}_1\left(1-\frac{T_m\beta(f_\kappa-\tilde{f}_v)}{(1+\epsilon_s)(1+Pr)(1-\tilde{f}_v)}\right)\right]}{\frac{\rho_m c_p|U_1|^2}{2\omega A_g(1-Pr)|1-f_v|^2}\Im\left[\tilde{f}_v+\frac{(f_\kappa-\tilde{f}_v)(1+\epsilon_s f_v/f_\kappa)}{(1+\epsilon_s)(1+Pr)}\right]-A_g k - A_s k_s} \tag{3}$$

$$\frac{d\dot{H}_2}{dx} = \dot{q} \tag{4}$$

In these equations, p_1 and U_1 are the first order amplitudes of the pressure and the volumetric velocity, respectively. T_m is the temperature. x is the axial direction of the system. $\dot{H}_2$ is the total energy flux. $\dot{q}$ is the gradient of $\dot{H}_2$, taken to be zero everywhere except at heat exchangers. Further, ρ_m, a, c_p, γ, β and Pr denote the mean density, the sound speed, the specific heat capacity, the specific heat ratio, the thermal expansion coefficient and the Prandtl number, respectively. ω is the angular frequency, k and k_s represent the thermal conductivity of the gas and solid, respectively, A_g and A_s represent the cross-sectional area for gas and solid, respectively. f_v and f_κ are spatially averaged functions for viscous and thermal effects. ε_s is a correction for thermal properties of the solid wall, accounting for the effect of solid on the acoustic oscillations together with the term $A_s k_s$. The symbols $\Re$ and $\Im$ denote the real and imaginary parts of a complex number. The tilde symbol represents the conjugate of a complex number.

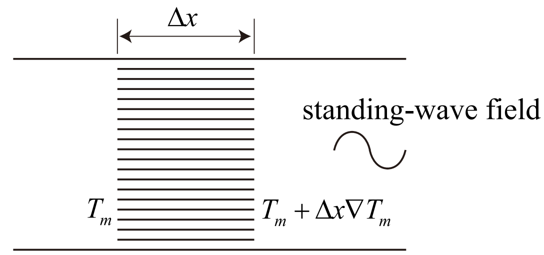

Fig. 1. The short engine model.

An important characteristic of the present model is the use of real fluid properties, which is obtained through NIST Refprop software [31], whose data have been validated against experimental measurements [32]. The temperature difference between solid and gas in heat exchangers was calculated based on the method described in Refs. [33] and [34].

2.2. The short engine approximation

The variation of acoustic power not only depends on fluid properties, but is also determined by the acoustic field (namely, p_1 and U_1). On the other hand, in actual thermoacoustic systems, p_1 and U_1 are strongly dependent on the geometry of the channel and the fluid properties, and they vary along the system. To exclude the influence of the acoustic field and isolate the effects of fluid properties near the critical point, following Swift [22], a short engine model is used. As shown in Fig. 1, the short engine is a stack with a length of Δx, which is so short that the acoustic field inside it can be considered uniform. All the other components, including the heat exchangers and resonators, are ignored, so that we can focus on the thermoacoustic conversion in the stack.

The variation of the acoustic wave passing through the short engine can be calculated by simply solving Eqs. (1) to (4), and the values of all the other related parameters in it can also be obtained. Specifically, the acoustic power generation by the short engine $\Delta\dot{E}$ can be expressed as

$$\Delta\dot{E} = -\frac{\Delta x}{2}\Re\left\{p_1\frac{d\tilde{U}_1}{dx}+\frac{dp_1}{dx}\tilde{U}_1\right\} \tag{5}$$

Thus the energy output density E_V is defined as

$$E_V = \Delta\dot{E}/V_{sh} \tag{6}$$

where V_{sh} is the volume of the short engine.

The input heat Q_h is calculated through energy balance [22]

$$Q_h = \dot{E}_h - \dot{H}_2 \tag{7}$$

where $\dot{E}_h$ and $\dot{H}_2$ represent the acoustic power at the hot end of the stack and the total energy flux right after the stack.

Therefore, the thermal efficiency η of the short engine is calculated by

$$\eta = \Delta\dot{E}/Q_h \tag{8}$$

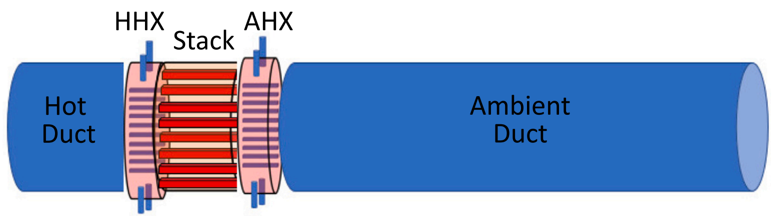

Fig. 2. Schematic of the standing-wave thermoacoustic engine, exported from PC-TAS [37].

Table 1
Critical temperatures and pressures of some fluids. T_{cr}-critical temperature. p_{cr}-critical pressure.

Items	T_{cr} (K)	p_{cr} (MPa)
CO_2	304.13	7.377
Ethane	305.32	4.872
R32	351.255	5.782
Propylene	364.21	4.555
Dimethylether(DME)	400.38	5.341

and the corresponding relative Carnot efficiency η_2 is

$$\eta_2 = \frac{\Delta \dot{E} T_h}{Q_h (T_h - T_c)} \tag{9}$$

From Eqs. (1), (2), (3), (5), (7) and (9), neglecting the heat conduction terms, it can be reached that the efficiency of the short engine is determined by seven parameters [35],

$$\eta_2 = \mathcal{F}\left(p_m, T_m, \nabla T_m/\omega, |z|, \varphi, \tau_\alpha, gas\right) \tag{10}$$

in which $\nabla T_m/\omega$ is the ratio of temperature gradient over angular frequency, $|z| = |p_1| A_g / |U_1|$ is the amplitude of the acoustic impedance. $\tau_\alpha = r_h \sqrt{\omega/\alpha}$ is the Womersley number, which can be considered a hydraulic radius of the stack scaled by the penetration depth. φ is the phase difference between p_1 and U_1, which is set to be 92°, a typical value in standing-wave engines [30].

CO_2 is used as the main working fluid, because its critical point is achievable in lab conditions, and subcritical and transcritical CO_2 has been widely used in conventional power cycles [36]. Additionally, some other fluids listed in Table 1 are also investigated.

2.3. Full-scale standing-wave engine

To gain more quantitatively accurate results, a simulation of a full-scale standing-wave thermoacoustic engine is also performed. The engine was modified from a representative engine developed by Swift [33] in 1992, to better suit the operation with near-critical fluids. As shown in Fig. 2, the engine consists of a hot duct, a hot heat exchanger (HHX), a stack, an ambient heat exchanger (AHX) and an ambient duct. The detailed dimensions of each component are presented in Table 2. We note that these dimensions are a result of an optimization procedure by a manual iterative process, for highest efficiency at $p_m/p_{cr} = 0.9$. Additionally, the ambient temperature is fixed at T_{cr}+5 K. This temperature was selected to ensure that the operating conditions are always above the critical temperature, so no multi-phase fluids are encountered. Again, CO_2 is used as the working fluid in most of the simulations.

The efficiency η for the engine is defined as the ratio of the generated acoustic power through the stack and the input heat (similar to Eq. (8)), while the corresponding relative Carnot efficiency η_2 is defined according to Eq. (9).

The system was modeled with the aid of the software PC-TAS [37], and the detailed methodology has been described in the appendix.

3. Validation of the model

In this section, the experimental data of the engine developed by Martinez et al. [26] are used as a benchmark to validate the model. As can be seen in Fig. 3, both the calculated values of the pressure amplitude $|p_1|$ and the frequency f show good agreements with the experimental results, indicating that the model is able to qualitatively capture the basic features of the operation of the engine. The calculated values of $|p_1|$ are slightly lower than the experimental data, with the deviations within 34%. The deviations decrease as p_m is increased. The low operating frequency (~5 Hz) reported by Martinez et al. [26] is due to the low sound speed in trans-critical fluids. It was accurately captured by the model, with deviations within 4% . The main reason for the deviations may be coil of the resonator and the sudden change in cross-sectional areas between thermoacoustic core and resonators, which introduced additional impedance and altered the acoustic field in the experiments, but was not considered in the model. In addition, the non-linear effects (harmonics, compressible flow effects, gravity, etc.) neglected in Eqs. (1) to (3) are expected to be more significant for near-critical fluids than ideal gases, due to the non-linearity of the equation of state. We note that the continuous curves are fitted from the calculated values that are discontinuous (see the appendix). The discontinuity may be caused by the numerical algorithm used by PC-TAS [38], but it also indicates the possible existence of several solution branches, i.e., bi-stability, which has already been observed in both experimental and numerical studies in many classical thermoacoustic engines[39,40]. It is likely that the non-linear properties of fluids near critical point increase the probability of bi-stability. In summary, these results prove that the model is a reliable tool to analyze and predict the performance of near-critical thermoacoustic engines.

4. Results and discussion

4.1. Properties investigation

In Fig. 4, the properties of CO_2 near the critical point are investigated. As widely known, the thermodynamic properties of fluids can show significant non-linearity near the critical point, which is exemplified with thermal expansion coefficient β, density ρ_m and Prandtl number Pr. The trends of β and Pr are similar. Both of them reach peak values when pressure approaches critical values. For $T_m/T_{cr} = 1$, the peak appears exactly at the critical pressure p_{cr}. As T_m is increased, the peak value drops, and the corresponding critical p_m increases gradually. β and Pr at the peaks can be much higher than in an ideal gas. For instance, at the critical point, β can be two orders of magnitude higher. A large β of fluids near the critical point is responsible for the enhanced thermoacoustic conversion, and the related advantages of engines adopting near-critical fluids. However, a high Pr, which indicates a more severe viscous loss, is detrimental [41]. As for the density ρ_m, there exists an abrupt change when p_m is increased across the critical value. Such change becomes less significant as temperature is increased further above the critical temperature.

According to Rott's thermoacoustic theory [30], the acoustic power variation in the engine along the axial direction can be calculated by

Table 2
Dimensions of the components of the thermoacoustic engine. HHX-hot heat exchanger, AHX-ambient heat exchanger. r_h-hydraulic radius. τ_α-defined as $r_h\sqrt{\omega/\alpha}$, where ω is the angular frequency, α is the thermal diffusivity. ψ-porosity.

Items	Diameter (mm)	Length (mm)	Details
Hot Duct	127	145	–
HHX	127	18	Parallel-plates type, ψ is 0.393, τ_α is 0.39.
Stack	127	84	Round pore, ψ is 0.81, τ_α is 1.4.
AHX	127	25	Parallel-plates type, ψ is 0.486, τ_α is 1.1.
Ambient Duct	127	3650	–

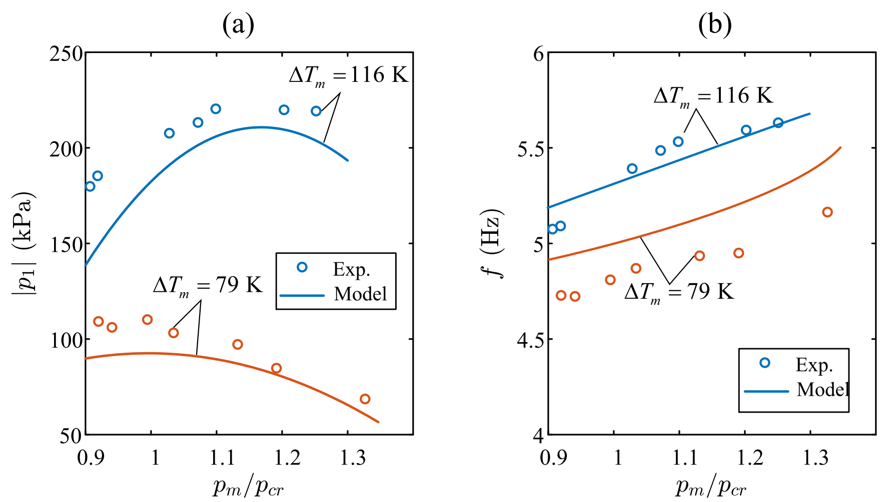

Fig. 3. Comparison between the experimental results in Martinez et al. [26] and the numerical results. (a) Pressure amplitude $|p_1|$. (b) Frequency f. The circles and the curves represent the experimental and numerical results, respectively.

$$\frac{d\dot{E}_2}{dx} = -\frac{r_v}{2}\left|U_1\right|^2 - \frac{1}{2r_\alpha}\left|p_1\right|^2 + \frac{1}{2}\Re\left[g\widetilde{p}_1 U_1\right] \tag{11}$$

in which r_v and r_α represent the acoustic resistances due to the viscous and the thermal-relaxation effects. g is the acoustic source term, which directly shows the effect of thermoacoustic conversion.

$$r_v = \frac{\omega\rho_m}{A_g}\frac{\Im\left[-f_v\right]}{\left|1-f_v\right|^2} \tag{12}$$

$$\frac{1}{r_\alpha} = (1-\gamma)\,\Im\left[f_\kappa\right]\frac{\omega A_g}{\rho_m a^2} \tag{13}$$

$$g = \frac{\left(f_\kappa - f_v\right)}{\left(1-f_v\right)(1-Pr)}\beta\nabla T_m \tag{14}$$

From Eq. (11), it is clear that the acoustic power generation is proportional to the source term g, while the viscous and thermal dissipations are proportional to the viscous resistance r_v and the thermal-relaxation resistance r_α, respectively. Hence, the variations of $|g|$, r_v and r_α are also shown in Fig. 4. It is obvious that they share similar trends: all of them go up as p_m is increased until reach peaks; these peaks are increasingly higher and the corresponding locations of the peaks are more and more close to p_{cr}, when T_m approaches T_{cr}. For $|g|$, its trend is dominated by the variations of β, which $|g|$ is proportional to according to Eq. (14); while for r_v and r_α, their trends are determined by the tendencies of both ρ_m and Pr. Since the influences of the rising $|g|$ and two resistances (r_v and r_α) on thermoacoustic conversion are contrary, their comprehensive effect on the performance of the engine can be intricate, and is determined by both the fluid properties and the local acoustic field.

4.2. The short engine

In this section, the performance of the short engine will be discussed. In Fig. 5, the dependence of the efficiency η_2 on Womersley number τ_α, with different acoustic impedance $|z|$ or different temperature gradients $\nabla T_m/\omega$, is shown. As widely known, for efficient standing-wave thermoacoustic conversion, imperfect thermal contact between the gas and the solid is required, otherwise the temperature difference between the gas and the solid in the adiabatic processes cannot be maintained [22]. Therefore, the optimal τ_α, which can be considered a dimensionless hydraulic radius of the channel, is between 1 to 1.5, depending on $|z|$. A relatively large $|z|$ helps decrease the viscous loss in the stack section. In this engine, the optimal $|z|$ for highest η_2 is around 10 $\rho_m a$. Moreover, increasing $\nabla T_m/\omega$ may help improve efficiency, but will decrease the generated acoustic power when $|z|$ is fixed. For instance, the efficiency η_2 is increased from 0.13 to 0.32 when $\nabla T_m/\omega$ decreases from 15.9 K s/m to 4.8 K s/m, but the generated acoustic power drops by nearly 90%. In the following discussion, $|z| = 10\ \rho_m a$ and $\nabla T_m/\omega = 4.8$ K s/m are chosen.

The thermoacoustic conversion near the critical point shows strong dependence on p_m and T_m. In Fig. 6, the performance of the short engine with different p_m and T_m is examined. Note that the optimal values of τ_α for various p_m and T_m are different (see the appendix). Hence, the values of τ_α have been optimized at every point, so the data can be considered the highest η_2 that a standing-wave engine can obtain with the specific $\nabla T_m/\omega$ and $|z|$. The positive effect of near-critical conditions on the standing-wave engine is clearly shown: it increases the output power of the engine, because the thermoacoustic conversion characterized by g is enhanced near the critical point (see Fig. 4). The benefit from a higher E_V is not only a larger power output, but also a lower temperature difference required to drive a full-scale engine. The reason behind this is that a larger E_V means a higher acoustic power generated in the stack under a fixed temperature difference in the engine, but the energy dissipation to be overcome for oscillation in the rest of the system changes slightly [42]. However, on the other hand, working near the critical point decreases the efficiency, because the viscous and thermal dissipation increases (this is quantified by the increase in r_v and r_α. See Fig. 4), and they dominate the change of efficiency. At the critical point, η_2 goes towards zero because of the very large viscous loss. When p_m exceeds p_{cr}, η_2 recovers in some degree, but it is still very low. This indicates that near the critical point, supercritical fluids may be not a

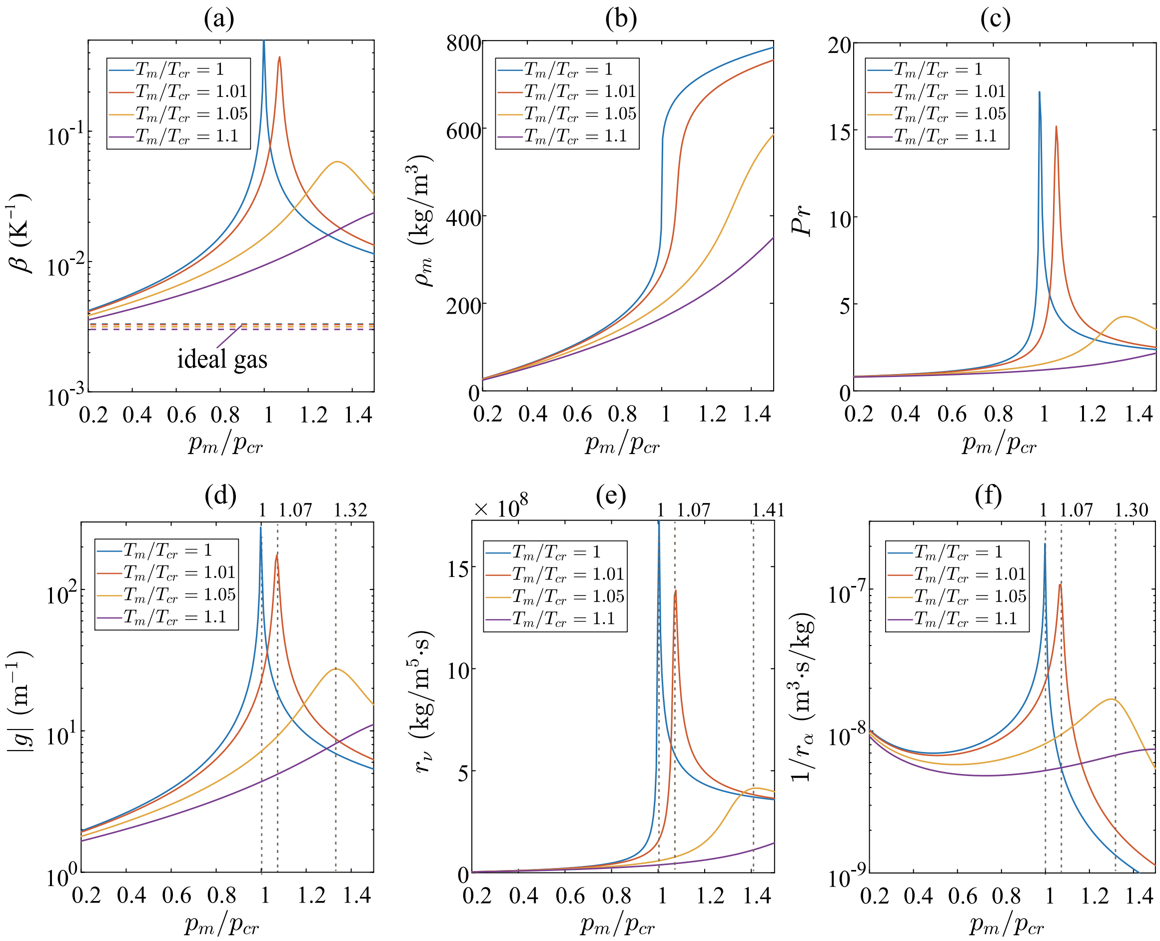

Fig. 4. Properties of CO_2 near the critical point. (a) Thermal expansion coefficient. (b) Density. (c) Prandtl number. (d) Acoustic source term. (e) Viscous resistance. (f) Thermal-relaxation resistance. In (d), (e) and (f), $A_g = 0.001$ m^3, $\nabla T_m = 600$ K/m and $f = 20$ Hz are arbitrarily set. They have no effect on the trends of the curves. τ_α is fixed at 1.4 by adjusting the hydraulic radius.

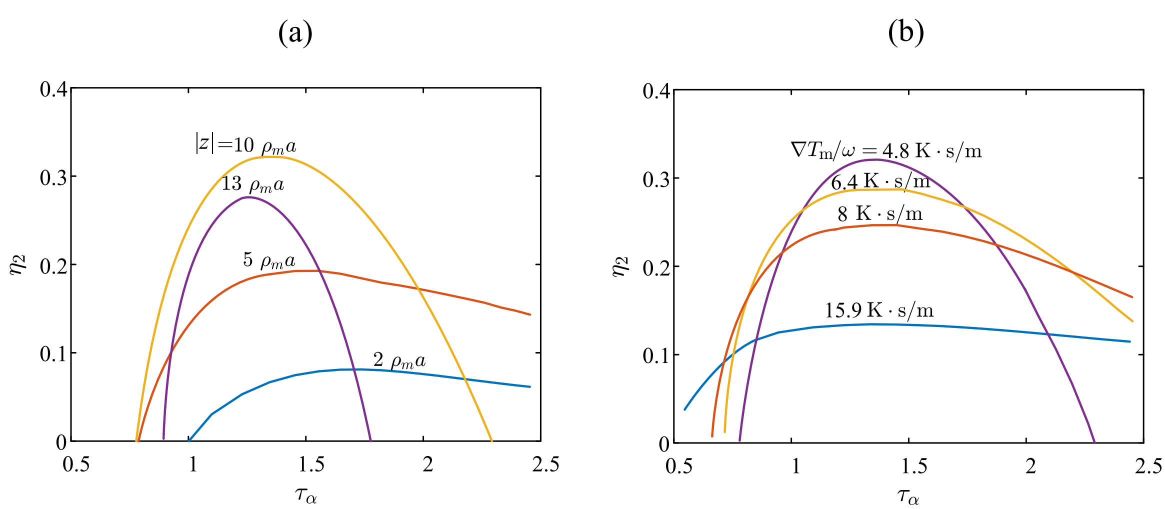

Fig. 5. Relative Carnot efficiency η_2 of the short engine vs. Womersley number τ_α, with different acoustic impedance $|z|$ in (a), or different $\nabla T_m/\omega$ in (b). $T_m = T_{cr}$, $p_m = 0.8p_{cr}$. $\tau_\alpha = r_h\sqrt{\omega/\alpha}$.

good choice. Therefore, we will focus on subcritical conditions in most of the discussion ($T_m > T_{cr}$ and $p_m < p_{cr}$).

In Fig. 7, the performances of the short engine with fluids listed in Table 1 in their subcritical conditions are presented. Again, the values of τ_α have been optimized at every point. T_m is set at T_{cr}. It can be seen that in all curves, η_2 drops towards zero when p_m is increased towards the critical point. However, the optimal p_m for highest η_2 are different. As mentioned above, the advantage of near-critical conditions is that they help increase the power output of the engine. This advantage is more significant for fluids with a lower p_{cr}, as reflected by the steeper curves of E_V near their critical pressures. For instance, E_V is doubled when p_m is increased from 3.7 MPa to 4.5 MPa (0.99 p_{cr}) for propylene;

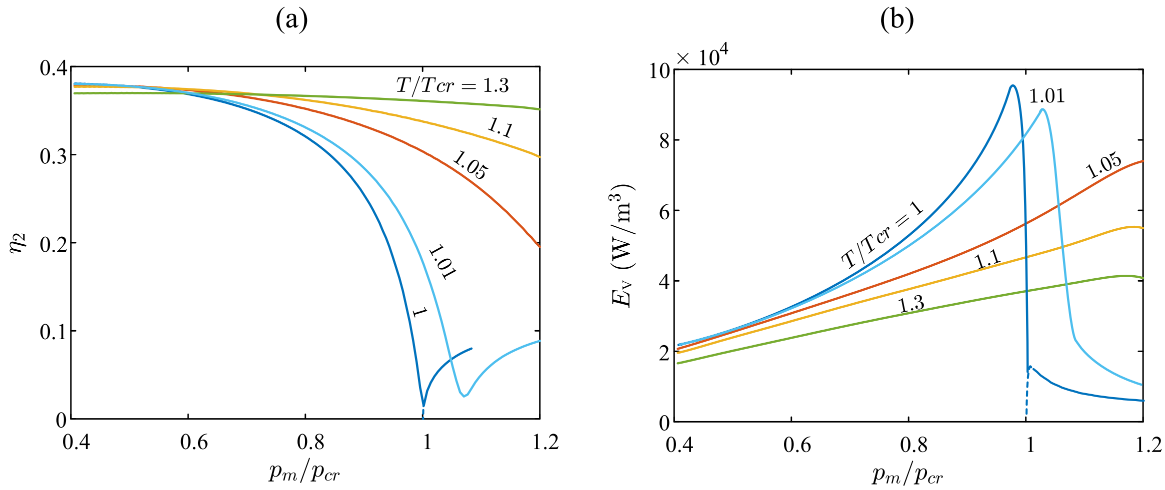

Fig. 6. Performance of the short engine under different mean pressures, with different temperatures. (a) Relative Carnot efficiency η_2. (b) Output power density E_V. $|z| = 10\ \rho_m a$. $\nabla T_m/\omega = 4.8$ K s/m.

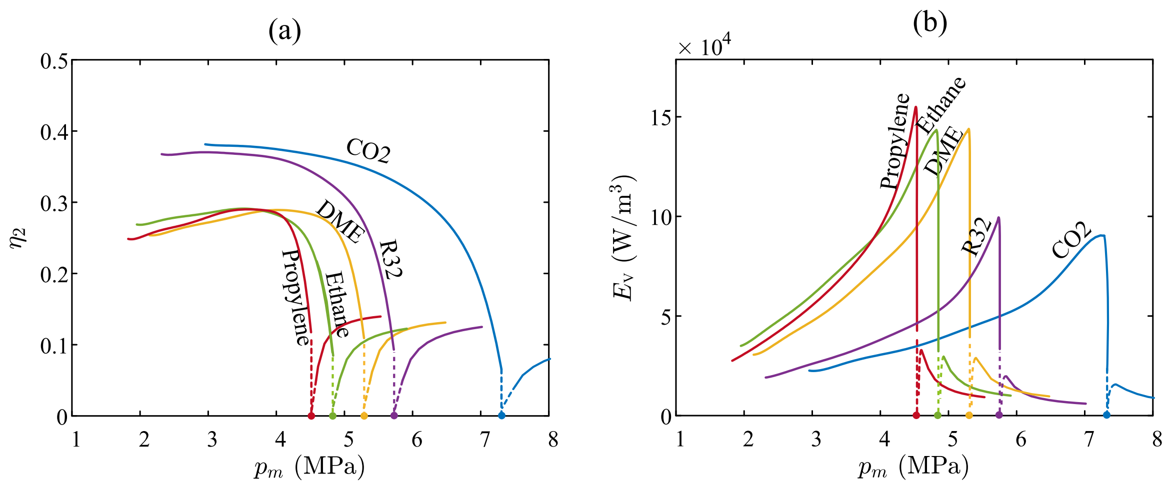

Fig. 7. Performance with a different mean pressure, for various fluids. (a) Relative Carnot efficiency η_2. (b) Output power density E_V. $|z| = 10\ \rho_m a$. $\nabla T_m/\omega = 4.8$ K s/m. $T = T_{cr}$. The location of the dashed line represent the critical pressure of each fluid.

however, for the same increase of p_m near the critical point, E_V only is slightly increased for CO_2. In general, the effects of the near-critical fluid is that it increases the power output, but it reduces the efficiency, so a trade-off needs to be reached to choose the fluid and the proper working conditions.

4.3. The full-scale engine

In this section, results for the full-scale standing-wave engine are discussed.

To demonstrate the advantages of a near-critical fluid over a gas far away from the critical point, in Fig. 8, the performance of engines with helium and CO_2 as the working gas is compared. Note that the helium engine is similar to the one developed by Swift [33], but with adjustment on hydraulic radius of the stack to better fit the mean pressure. The mean pressure is scaled by the critical pressure of CO_2. The relative Carnot efficiency η_2 shows strong dependence on p_m when CO_2 is used. When p_m is increased towards p_{cr}, both the thermoacoustic conversion (specified by the source term $|g|$) and the acoustic dissipation (specified by the viscous resistance r_ν and the thermal-relaxation resistance r_α) are significantly increased (see Fig. 4 for details). Their trade-off, which is also affected by the local acoustics, determines the variation of η_2. Specifically, when p_m is increased towards p_{cr}, η_2 rises until reaches a peak at around $p_m/p_{cr} = 0.79$, where the temperature difference ΔT_m reaches the lowest value. However, when p_m/p_{cr} is further increased, η_2 drops and ΔT_m rises, until p_m/p_{cr} reaches 1.09. Basically, the trends match those in the short engine model in Fig. 6. The peak efficiency appears at $p_m/p_{cr} = 0.79$, higher than that in the short engine model, because of the specific system design: this engine was optimized under $p_m/p_{cr} = 0.9$. Since a lower p_m helps increase efficiency (see Fig. 6), it is reasonable that the peak appears at a lower mean pressure. For comparison, the performance of the engine with helium shows a much weaker dependence on p_m because the engine works far away from the critical point of helium ($T_{cr} = 5.20$ K, $p_{cr} = 0.227$ MPa). Additionally, the curves for the three input heat are similar. The highest η_2 of CO_2 is 0.28, which is comparable to that of helium; meanwhile, the temperature difference ΔT_m is much lower than that required for helium. This indicates the advantages of near-critical fluids for low-grade heat recovery.

As indicated by the discussion in Section 4.2 (see also Fig. 6), one of the potential advantages of near-critical fluids is the high power output. To verify this, in Fig. 9, the performance of the engine with various input heat Q_h is presented. It is clear that the generated acoustic power $\Delta \dot{E}_s$ and the temperature difference ΔT_m increase with the rise of input heat Q_h. η_2 grows as Q_h is increased from about 100 W, until reaches a peak of 0.285 (with the corresponding η of 0.06) at around $Q_h = 800$ W. Then η_2 decreases gradually as Q_h is further increased. When Q_h is 10 kW, η_2 becomes 0.25. A main reason for the decreased efficiency

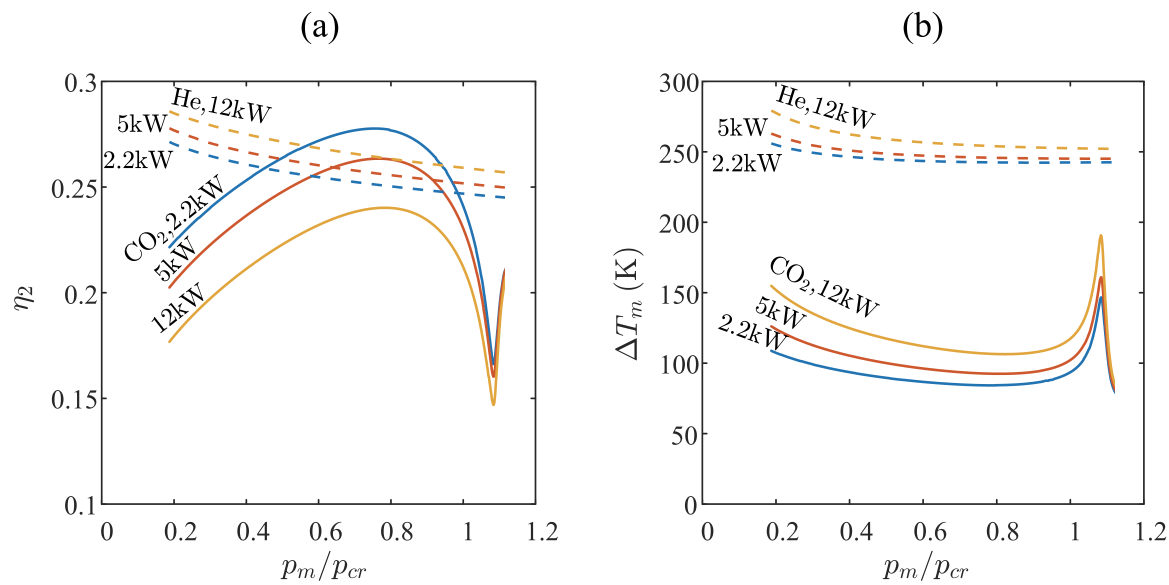

Fig. 8. Performance comparison of the engine with CO_2 and helium as working fluid respectively, under different mean pressure. (a) Relative Carnot efficiency η_2. (b) Temperature difference ΔT_m. Results for three different input heat, i.e., 2.2 kW, 5 kW and 12 kW, are given. p_{cr} is the critical pressure of CO_2, which is 7.38 MPa. T_a=308 K.

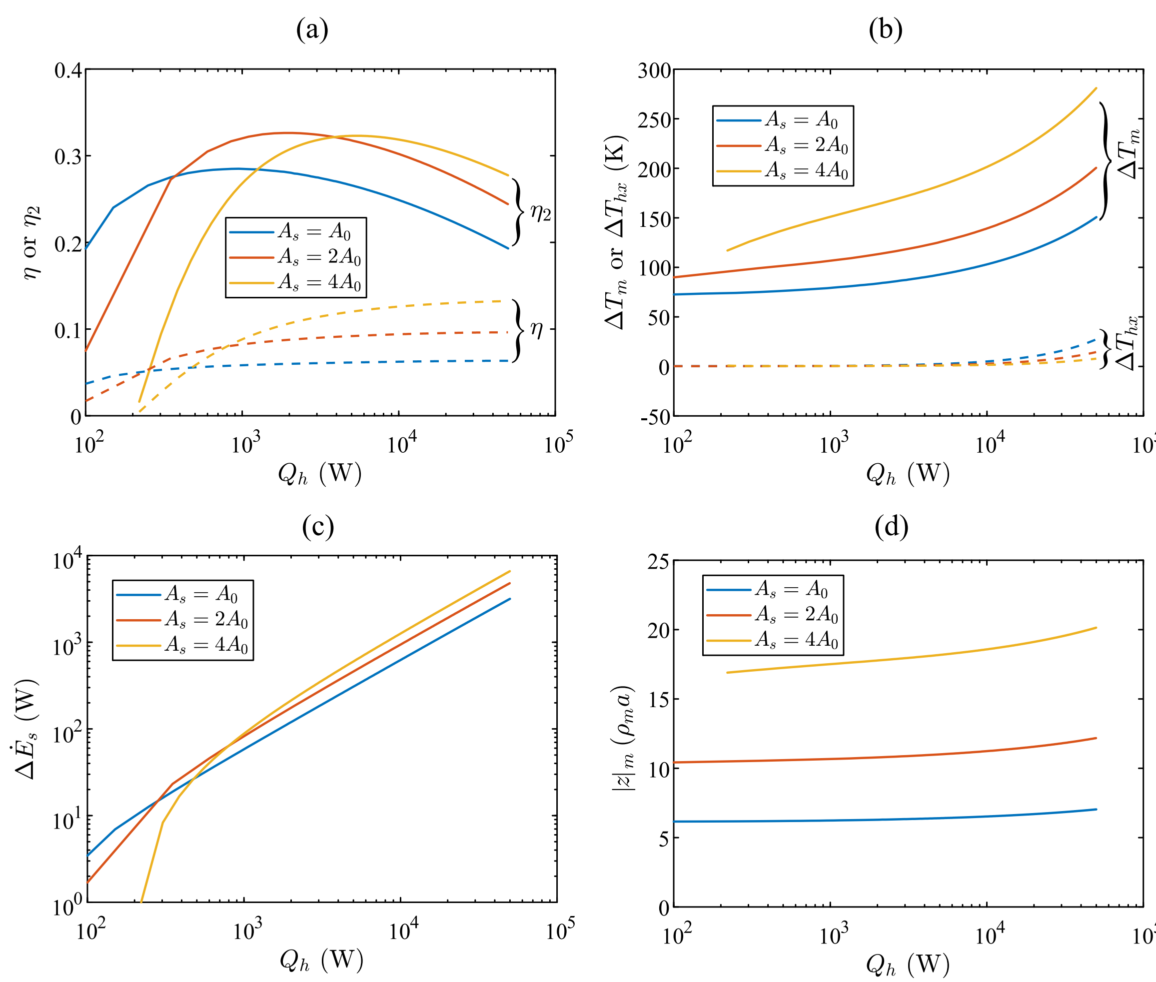

Fig. 9. Performance of the engine with various input heat Q_h. (a) Thermal efficiency η or relative Carnot efficiency η_2. (b) Temperature difference ΔT_m or gas-solid temperature difference in two heat exchangers ΔT_{hx}. (c) Generated acoustic power $\Delta \dot{E}_s$. (d) Mean acoustic impedance in the stack $|z|_m$. Results for three different cross-sectional area of the stack A_s are given. A_0 is the original cross-sectional area.

is the growth of viscous loss, which is proportional to the square of velocity amplitude $|v_1|$ [30]. Therefore, to improve the efficiency of the system under a higher Q_h, a practical technique is to enlarge the cross-sectional area of the stack, so that the acoustic impedance can be

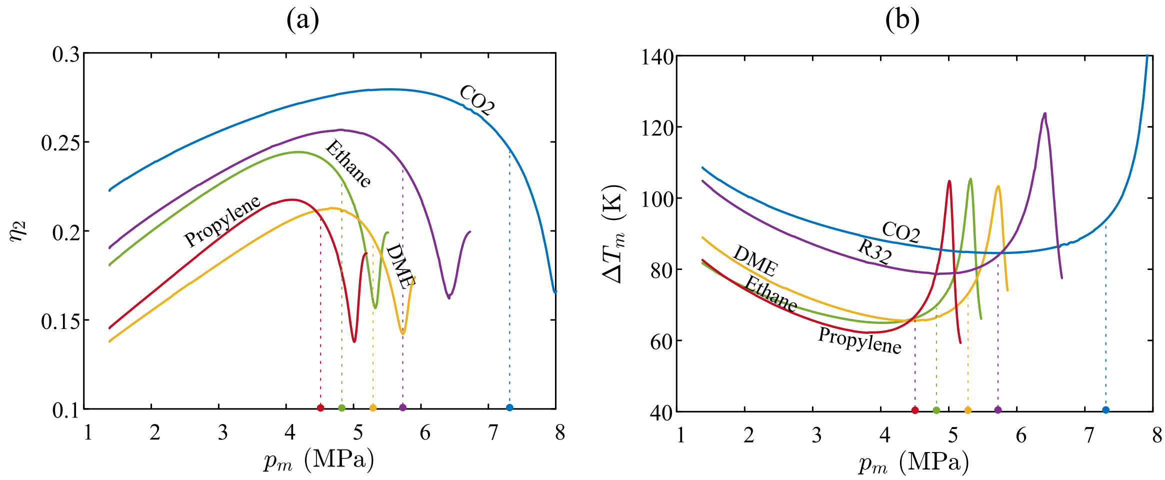

Fig. 10. Performance of the engine under different mean pressure, with different fluids. (a) Relative Carnot efficiency η_2. (b) Temperature difference ΔT_m required to drive the engine. The location of the dashed line represents the critical pressure for each fluid. Q_h is fixed at 2.2 kW.

increased, and the viscous loss can be reduced [43]. In Fig. 9, the results with $A_s = 2A_0$ and $A_s = 4A_0$ are also shown, where A_0 is the cross-sectional area of the original design. The values of Q_h with which η_2 peaks is increased to 1.8 kW and 5.7 kW when $A_s = 2A_0$ and $A_s = 4A_0$, respectively, with the corresponding peak η_2 being 0.326 and 0.323. The mean acoustic impedance along the stack $|z|_m$ are 6.2 $\rho_m a$, 10.7 $\rho_m a$ and 17.6 $\rho_m a$ with $A_s = A_0$, $A_s = 2A_0$ and $A_s = 4A_0$, respectively, when Q_h is about 1 kW. Importantly, for low-temperature-difference thermoacoustic engines, a main obstacle for the operation with high energy density is the increasingly high temperature difference between gas and solid in the heat exchanger [44]. As can be seen in subfigure (b), this problem can be significantly mitigated by using near-critical fluids. The temperature difference between solid and gas in both heat exchangers is much lower than usually seen in classical thermoacoustic engines, even with heat inputs as high as 10 kW. This is due to the high heat capacity $\rho_m c_p$ of near-critical CO_2, which significantly enhances the heat transfer between gas and solid.

In Fig. 10, the influence of different fluids on the performance of the engine, specified by the relative Carnot efficiency η_2 and the temperature difference required to drive the engine, is demonstrated, under different mean pressure p_m. The location of the dashed line represents p_{cr} for each fluid. It can be seen that the trends for all fluids are similar: values of η_2 decrease as p_m is increased towards p_{cr}, reach peaks below and near p_{cr} of each fluid, and drop when p_m is further increased; meanwhile, the curves for ΔT_m have opposite trends. This confirms the effect of the near-critical point on the performance of the engine, which is reducing the temperature difference but lowering the efficiency. Further, the comparison between Fig. 10(b) and Fig. 7(b) verifies the deduction that a higher E_V helps reduce ΔT_m, which was proposed in the discussion of the short engine. As for the variation of η_2 between different substances under a fixed p_m, it basically matches that in Fig. 7. For instance, CO_2 enjoys the highest η_2, and is followed by R32. However, the difference in η_2 of the three other fluids is more significant than that in the short engine, because of the specific engine design, and the fixed input heat. Additionally, the negative peak is at a pressure slightly higher than p_{cr}, while in the short engine model, the lowest η_2 appears at p_{cr}. The reason is that the lowest temperature in the engine is above T_{cr}, and the temperature is not fixed along the stack.

5. Conclusions

In this work, thermoacoustic conversion was investigated, theoretically, for fluids near the critical point — extending the commonly assumed ideal gas properties. The formulated model was validated against existing experimental results, showing good agreement. In the simulation, the operating temperature range of the whole system is above T_{cr} (the critical temperature), while the pressure is in the range of 0.2 p_{cr} to 1.2 p_{cr}, where p_{cr} is the critical pressure. The following conclusions can be reached:

First, from the short engine analysis, when pressure is increased or temperature is decreased towards the critical point, thermoacoustic conversion can be enhanced, but this is offset by acoustic dissipation, which also becomes more severe. As a result, the output power of the short engine increases but efficiency drops when the temperature gradient stays fixed. This is due to sudden changes of properties near the critical points, which increase both the acoustic source term and the acoustic dissipation from viscosity and thermal relaxation. These two factors show competing effects on the performance of the engine. Their trade-off, together with the acoustic field distribution, ultimately determines the efficiency.

Second, at supercritical temperatures, the sub-critical region (pressure slightly lower than p_{cr}) is better than the supercritical region near the critical point. This conclusion is obtained from the short engine model, and further verified in the full-scale engine model. Specifically, $p_m \sim 0.8\ p_{cr}$ is suggested. For the presented full-scale system, the relative Carnot efficiency is 0.26 when $p_m = 0.79\ p_{cr}$, which then drops to 0.16 when $p_m = 1.09\ p_{cr}$.

Importantly, a potential application of the near-critical thermoacoustic engine is low-grade heat recovery, due to the lower temperature difference required for operation and the enhanced heat exchanger performance. This is similar to some power cycles adopting trans-critical working fluids [45,46]. The technical difficulty of developing such a system is similar to classical thermoacoustic system, except the requirement of a charging device. This can be done through a bladder accumulator or some blower device [26].

Declaration of competing interest

The authors declare that they have no known competing financial interests or personal relationships that could have appeared to influence the work reported in this paper.

Data availability

Data will be made available on request.

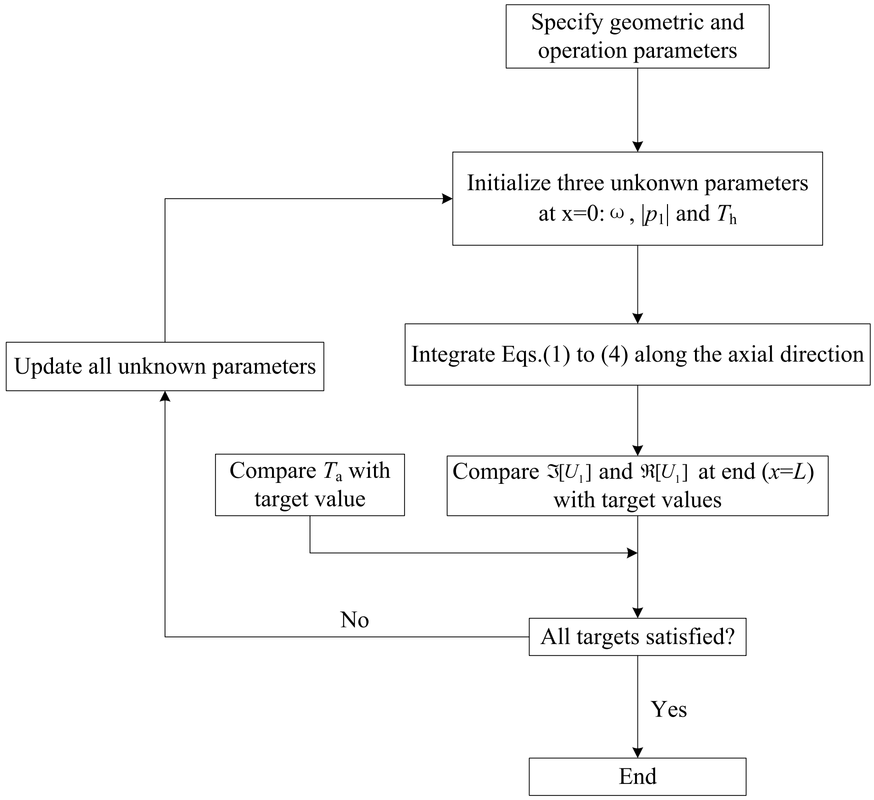

Fig. A.1. Methodology of the numerical algorithm for the full-scale engine.

Acknowledgments

N.B would like to thank the Grand Technion Energy Program and the Jacobs fellowship for their support.

Appendix A. Assumptions of the theory

The assumptions made in the model are called the Rott's acoustic approximations [30], including the following items:

(a) The acoustic wave propagates only in one direction (x direction).

(b) The wavelength is much longer than the penetration depths.

(c) System variables are considered to be the sum of an average and time-periodic quantities, which oscillate sinusoidally,

$$p(x,t) = p_m + \Re\left[p_1(x)e^{i\omega t}\right]$$
$$u(x,y,z,t) = \Re\left[u_1(x,y,z)e^{i\omega t}\right]$$
$$T(x,y,z,t) = T_m(x) + \Re\left[T_1(x,y,z)e^{i\omega t}\right]$$
$$\rho(x,y,z,t) = \rho_m(x) + \Re\left[\rho_1(x,y,z)e^{i\omega t}\right]$$

where higher-order terms are neglected. In the above equations, the subscripts "m" and "1" represent the mean and first order, oscillating values, respectively.

(d) For parameters like T and ρ, the first order values are much smaller than the corresponding mean values. For u, it is much smaller than sound speed.

Appendix B. Methodology of the full-scale engine

The methodology of numerical solution is shown in Fig. A.1. After specify geometric and operation parameters of the system, the governing equations (i.e., Eqs. (1) to (4)) can be integrated along the axial direction with a fourth-order Runge-Kutta method. However, the angular frequency ω, the pressure amplitude p_1 at the beginning of the integration ($x = 0$) and the hot temperature T_h are unknown. To perform the integration, their initial values were given artificially. To obtain precise values of unknown parameters, three targets needs to be satisfied, which are:

$$\Re\left[U_1\right]\Big|_{x=L} = 0 \tag{A.2a}$$

$$\Im\left[U_1\right]\Big|_{x=L} = 0 \tag{A.2b}$$

$$T_h = \text{target value} \tag{A.2c}$$

Aided by a shooting method and targeting the three boundary conditions, the problem is solved. As a result, the distributions of p_1, U_1, T_m and other parameters can also be obtained. All the calculations are done using PC-TAS, a software for simulating thermoacoustic systems [37].

A more detailed description on how the PC-TAS works can be found in its users' guide (https://wetlab.net.technion.ac.il/files/2023/03/PCTAS-Users-Guide.pdf). The source code of PC-TAS, including the modified code used for this paper, can be found in https://wetlab.net.technion.ac.il/pc-tas/. We also note that running a system with non-ideal fluids requires the installation of NIST Refprop, and the MATLAB-Refprop interface (https://github.com/usnistgov/REFPROP-wrappers/blob/master/wrappers/MATLAB/legacy/refpropm.m).

Appendix C. Supplementary data for Fig. 3

In Fig. A.2, we show both the original discontinuous results from calculation and the fitted curve.

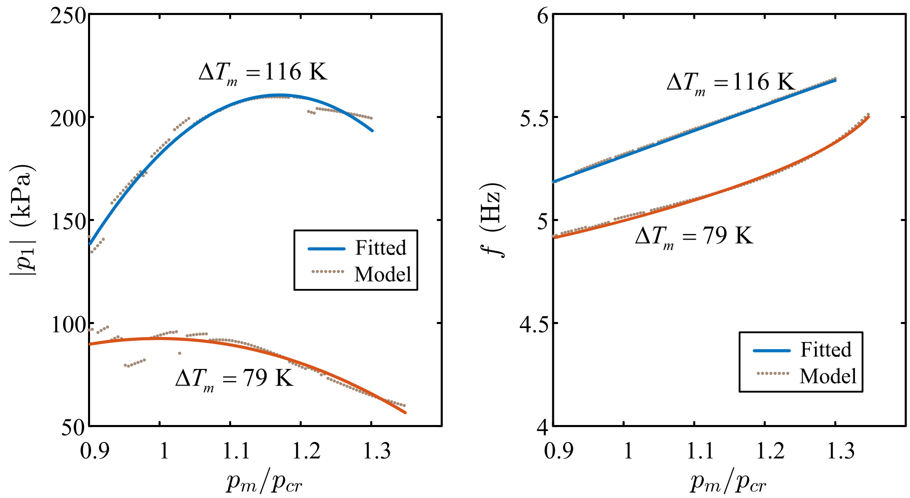

Fig. A.2. The original results for calculation and the fitted curve.

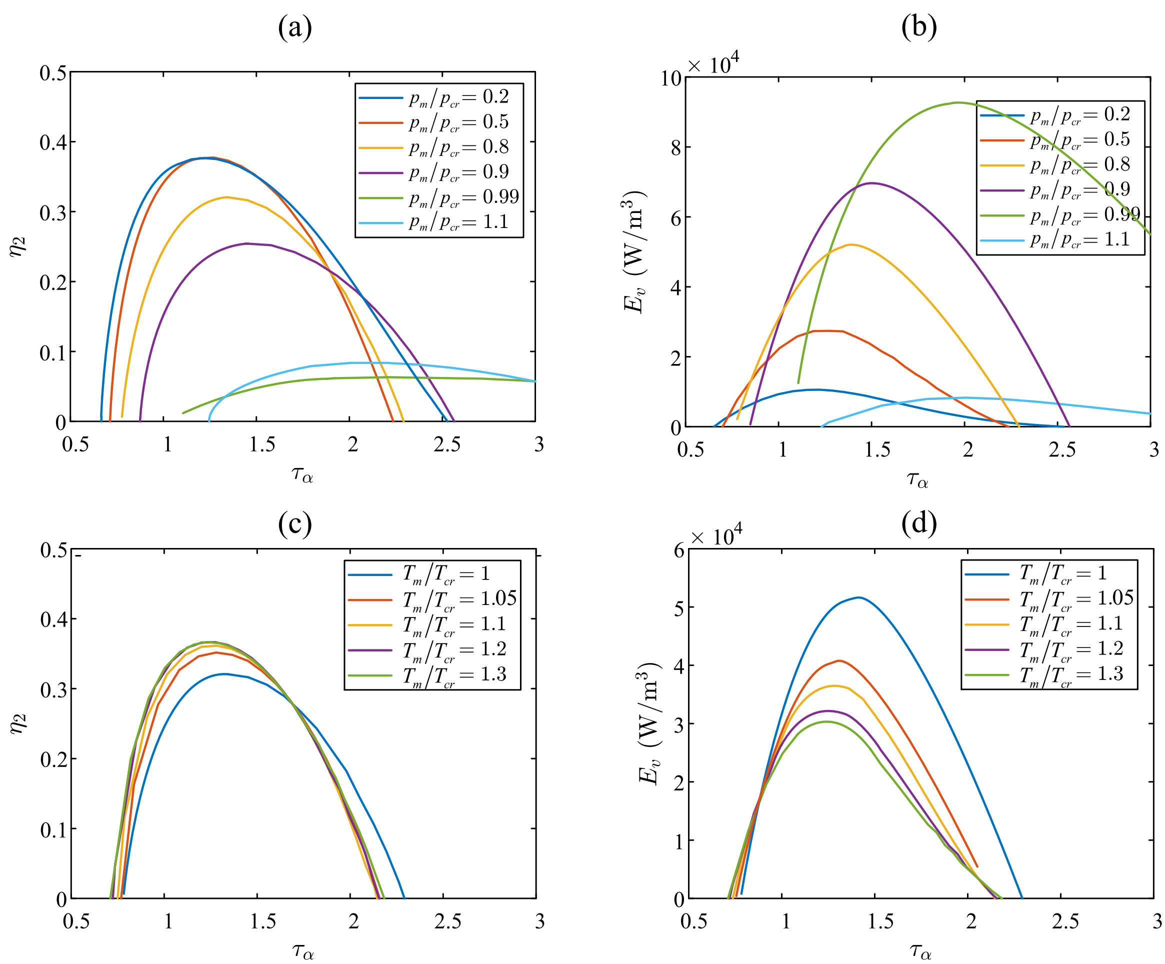

Fig. A.3. Relative Carnot efficiency η_2 and output power density E_V of the short engine vs. Womersley number τ_α. In (a) and (b), results for different p_m/p_{cr} are shown, with $T_m/T_{cr} = 1$. In (c) and (d), results for different T_m/T_{cr} are shown, with $p_m/p_{cr} = 0.8$. $|z| = 10\ \rho_m a$. $\nabla T_m/\omega = 4.8$ K s/m. $\tau_\alpha = r_h\sqrt{\omega/\alpha}$.

Appendix D. Supplementary data for the short engine

To investigate the effect of near-critical working conditions, in Fig. A.3, the performance of the short engine, specified by the relative Carnot efficiency η_2 and output power density E_V, is shown under different p_m, and T_m.

Appendix E. Distributions of parameters in the stack

In Fig. A.4, three points from Fig. 8, which are $p_m/p_{cr} = 0.19$, $p_m/p_{cr} = 0.79$ and $p_m/p_{cr} = 1.09$ for CO_2, are selected to show their distributions of T_m/T_{cr}, $\dot{E}_2$, β and Pr on the stack.

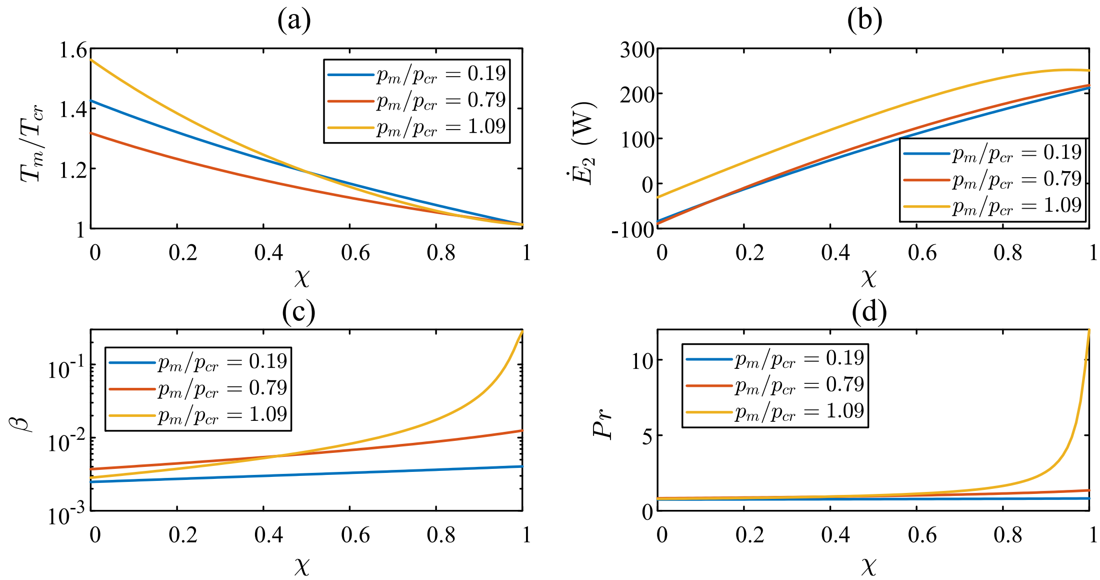

Fig. A.4. Distributions of various parameters along the stack. (a) Scaled temperature T_m/T_{cr}. (b) Acoustic power $\dot{E}_2$. (c) Thermal expansion coefficient β. (d) Prandtl number Pr. The three cases are selected from Fig. 8. χ is the dimensionless location on the stack. $\chi = 0$ and $\chi = 1$ represent the hot and cold ends of the stack respectively.

References

[1] G. Chen, L. Tang, B. Mace, Z. Yu, Multi-physics coupling in thermoacoustic devices: A review, Renew. Sustain. Energy Rev. 146 (2021) 111170, http://dx.doi.org/10.1016/j.rser.2021.111170.

[2] G. Chen, J. Xu, Development of a small-scale piezoelectric-driven thermoacoustic cooler, Appl. Therm. Eng. (2022) 118667.

[3] S. Backhaus, G.W. Swift, A thermoacoustic Stirling heat engine, Nature 399 (6734) (1999) 335–338.

[4] T.W. Steiner, M. Hoy, K.B. Antonelli, M. Malekian, G.D. Archibald, T. Kanemaru, W. Aitchison, B. de Chardon, K.T. Gottfried, M. Elferink, et al., High-efficiency natural gas fired 1 kWe thermoacoustic engine, Appl. Therm. Eng. 199 (2021) 117548.

[5] M.E.H. Tijani, S. Spoelstra, A high performance thermoacoustic engine, J. Appl. Phys. 110 (9) (2011) 093519.

[6] R. Yang, Y. Wang, T. Jin, Y. Feng, K. Tang, Development of a three-stage looped thermoacoustic electric generator capable of utilizing heat source below 120 C, Energy Convers. Manage. 155 (2018) 161–168.

[7] J. Chi, Y. Yang, Z. Wu, R. Yang, P. Li, J. Xu, L. Zhang, J. Hu, E. Luo, Numerical and experimental investigation on a novel heat-driven thermoacoustic refrigerator for room-temperature cooling, Appl. Therm. Eng. 218 (2023) 119330.

[8] A. Al-Kayiem, Z. Yu, Using a side-branched volume to tune the acoustic field in a looped-tube travelling-wave thermoacoustic engine with a RC load, Energy Convers. Manage. 150 (2017) 814–821.

[9] G. Chen, J. Xu, Acoustic characteristics of looped-tube thermoacoustic refrigerators with external and in-built acoustic drivers: A comparative study, J. Acoust. Soc. Am. 150 (6) (2021) 4406–4416.

[10] D.R. Kassoy, The response of a confined gas to a thermal disturbance. I: Slow transients, SIAM J. Appl. Math. 36 (3) (1979) 624–634.

[11] I. Pioro, S. Mokry, Thermophysical properties at critical and supercritical conditions, Heat Transf.-Theoretical Anal. Exp. Investig. Ind. Syst. 22 (2011) 654.

[12] S.A. Hunt, M.T. Migliorino, C. Scalo, S.D. Heister, Onset Criteria for Bulk-Mode Thermoacoustic Instabilities in Supercritical Hydrocarbon Fuels, J. Fluids Eng. 143 (4) (2021) 040901, http://dx.doi.org/10.1115/1.4049401.

[13] W.S. Hines, H. Wolf, Pressure oscillations associated with heat transfer to hydrocarbon fluids at supercritical pressures and temperatures, Ars J. 32 (3) (1962) 361–366.

[14] D. Linne, M. Meyer, D. Braun, D. Keller, Investigation of instabilities and heat transfer phenomena in supercritical fuels at high heat flux and temperatures, in: 36th AIAA/ASME/SAE/ASEE Joint Propulsion Conference and Exhibit, 2000, p. 3128.

[15] B. Zappoli, S. Amiroudine, P. Carles, J. Ouazzani, Thermoacoustic and buoyancy-driven transport in a square side-heated cavity filled with a near-critical fluid, J. Fluid Mech. 316 (1996) 53–72, http://dx.doi.org/10.1017/S0022112096000444.

[16] B. Zappoli, A. Jounet, S. Amiroudine, A. Mojtabi, Thermoacoustic heating and cooling in near-critical fluids in the presence of a thermal plume, J. Fluid Mech. 388 (1999) 389–409.

[17] Z. Lei, B. Farouk, E.S. Oran, Numerical simulation of 'piston effect' in supercritical carbon dioxide, in: Heat Transfer Summer Conference, 47330, 2005, pp. 805–810.

[18] A. Onuki, Thermoacoustic effects in supercritical fluids near the critical point: Resonance, piston effect, and acoustic emission and reflection, Phys. Rev. E 76 (6) (2007) 061126.

[19] P. Carlès, Thermoacoustic waves near the liquid-vapor critical point, Phys. Fluids 18 (12) (2006) 126102.

[20] N. Hasan, B. Farouk, Thermoacoustic transport in supercritical fluids at near-critical and near-pseudo-critical states, J. Supercrit. Fluids 68 (2012) 13–24.

[21] J.C. Wheatley, W. Swift, A. Migliori, The natural heat engine, 1986, p. 32.

[22] G.W. Swift, Thermoacoustic engines, J. Acoust. Soc. Am. 84 (4) (1988) 1145–1180.

[23] T. Jin, R. Yang, K. Tang, An analysis of the influence of near-critical CO2 on performance of thermoacoustic resonator, Kung Cheng Je Wu Li Hsueh Pao/J. Eng. Thermophys. 35 (7) (2014) 1285–1289.

[24] M.T. Migliorino, Numerical and Theoretical Modeling of Thermoacoustic Instabilities in Transcritical Fluids (Ph.D. thesis), Purdue University Graduate School, 2019.

[25] M.T. Migliorino, C. Scalo, Real-fluid effects on standing-wave thermoacoustic instability, J. Fluid Mech. 883 (2020) A23, http://dx.doi.org/10.1017/jfm.2019.856.

[26] A.G. Martinez, B. Kuras, M. Tindaro Migliorino, C. Scalo, S.D. Heister, Experimental demonstration of high-amplitude thermoacoustic instabilities under transcritical temperature conditions in a standing-wave device, in: AIAA Scitech 2021 Forum, American Institute of Aeronautics and Astronautics, VIRTUAL EVENT, 2021, http://dx.doi.org/10.2514/6.2021-1175.

[27] A. Martinez, M.T. Migliorino, C. Scalo, S.D. Heister, Experimental and numerical investigation of standing-wave thermoacoustic instability under transcritical temperature conditions, J. Acoust. Soc. Am. 150 (4) (2021) 2900–2911, http://dx.doi.org/10.1121/10.0006659.

[28] D. Alexander, M.T. Migliorino, S. Heister, C. Scalo, Numerical and experimental analysis of a transcritical thermoacoustic prototype, in: 2018 Fluid Dynamics Conference, American Institute of Aeronautics and Astronautics, Atlanta, Georgia, 2018, http://dx.doi.org/10.2514/6.2018-3536.

[29] G. Swift, A. Migliori, T. Hofler, J. Wheatley, Theory and calculations for an intrinsically irreversible acoustic prime mover using liquid sodium as primary working fluid, J. Acoust. Soc. Am. 78 (2) (1985) 767–781.

[30] G.W. Swift, Thermoacoustics: a Unifying Perspective for Some Engines and Refrigerators, American Institute of Physics Press, New York, 2002.

[31] E.W. Lemmon, I. Bell, M.L. Huber, M.O. McLinden, NIST Standard Reference Database 23: Reference Fluid Thermodynamic and Transport Properties-REFPROP, Version 10.0, National Institute of Standards and Technology, 2018, http://dx.doi.org/10.18434/T4/1502528, URL https://www.nist.gov/srd/refprop.

[32] R. Span, W. Wagner, A new equation of state for carbon dioxide covering the fluid region from the triple-point temperature to 1100 K at pressures up to 800 MPa, J. Phys. Chem. Ref. Data 25 (6) (1996) 1509–1596.

[33] G.W. Swift, Analysis and performance of a large thermoacoustic engine, J. Acoust. Soc. Am. 92 (3) (1992) 1551–1563.

[34] W.C. Ward, G.W. Swift, Design environment for low-amplitude thermoacoustic engines, J. Acoust. Soc. Am. 95 (6) (1994) 3671–3672.

[35] R. Yang, N. Blanc, G.Z. Ramon, Theoretical performance characteristics of a travelling-wave phase-change thermoacoustic heat pump, Energy Convers. Manage. 254 (2022) 115202, http://dx.doi.org/10.1016/j.enconman.2021.115202.

[36] J.-Q. Guo, M.-J. Li, Y.-L. He, T. Jiang, T. Ma, J.-L. Xu, F. Cao, A systematic review of supercritical carbon dioxide (s-CO2) power cycle for energy industries: Technologies, key issues, and potential prospects, Energy Convers. Manage. (2022) 115437.

[37] R. Yang, N. Blanc, A. Vardi-Chouchana, N. Ouzana, G.Z. Ramon, PC-TAS: A design environment for phase-change and classical thermoacoustic systems, SoftwareX 19 (2022) 101142.

[38] F. Ling, Quasi-periodic solutions calculated with the simple shooting technique, J. Sound Vib. 144 (2) (1991) 293–304, http://dx.doi.org/10.1016/0022-460X(91)90750-E, URL https://www.sciencedirect.com/science/article/pii/0022460X9190750E.

[39] G. Chen, L. Tang, B.R. Mace, Bistability and triggering in a thermoacoustic engine: A numerical study, Int. J. Heat Mass Transfer 157 (2020) 119951.

[40] G. Chen, T. Jin, Experimental investigation on the onset and damping behavior of the oscillation in a thermoacoustic prime mover, Cryogenics 39 (10) (1999) 843–846.

[41] M.E.H. Tijani, J.C.H. Zeegers, A.T.A.M. de Waele, Prandtl number and thermoacoustic refrigerators, J. Acoust. Soc. Am. 112 (1) (2002) 134–143, http://dx.doi.org/10.1121/1.1489451.

[42] T. Biwa, D. Hasegawa, T. Yazaki, Low temperature differential thermoacoustic Stirling engine, Appl. Phys. Lett. 97 (3) (2010) 034102, http://dx.doi.org/10.1063/1.3464554.

[43] R. Yang, N. Blanc, G.Z. Ramon, Environmentally-sound: An acoustic-driven heat pump based on phase change, Energy Convers. Manage. 232 (2021) 113848.

[44] R. Yang, A. Meir, G.Z. Ramon, A standing-wave, phase-change thermoacoustic engine: Experiments and model projections, Energy 258 (2022) 124665.

[45] G. Manente, F.M. Fortuna, Supercritical CO2 power cycles for waste heat recovery: A systematic comparison between traditional and novel layouts with dual expansion, Energy Convers. Manage. 197 (2019) 111777, http://dx.doi.org/10.1016/j.enconman.2019.111777.

[46] K. Braimakis, M. Preißinger, D. Brüggemann, S. Karellas, K. Panopoulos, Low grade waste heat recovery with subcritical and supercritical Organic Rankine Cycle based on natural refrigerants and their binary mixtures, Energy 88 (2015) 80–92.